Dark and bright autoionizing states in resonant high-order harmonic generation: Simulation via a one-dimensional helium model

V. V. Strelkov ●[*]

Prokhorov General Physics Institute of the Russian Academy of Sciences, Vavilova Street 38, Moscow 119991, Russia;
Institute of Applied Physics of the Russian Academy of Sciences, 46 Ulyanov Street, Nizhny Novgorod 603950, Russia;
and Moscow Institute of Physics and Technology (National Research University), 9 Institutskiy Pereulok, Dolgoprudny 141701, Russia

We study the role of dark and bright autoionizing states (AISs) in photoionization and high-order harmonic generation (HHG) using a one-dimensional helium model. This model allows numerical integration of the time-dependent Schrödinger equation beyond the single-electron approximation, completely taking into account electronic correlation. We find the level structure of the system and the spatial distribution of the electronic density for several states, including AIS. Studying the HHG efficiency as a function of the detuning from the resonances with AISs, we find the HHG enhancement lines. The shapes of these lines are different from the corresponding Fano lines in photoelectronic spectra, in agreement with experimental studies on HHG in helium. Moreover, we simulate HHG under the conditions when the fundamental frequency is close to the even-order multiphoton resonance with the dark AIS. We find enhanced generation of the neighboring odd harmonics. The details of the enhancement lines for these harmonics can be understood by taking into account the temporal delay between the nonresonant and resonant XUV emissions; this delay is defined by the AIS lifetime. Finally, our simulations show that resonances with dark and bright AISs enhance HHG to a similar extent.

I. INTRODUCTION

Two-electron atoms are probably the simplest systems where electronic correlations play a crucial role. Schrödinger's equation describing correlated three-body Coulomb dynamics cannot be resolved analytically; several approximate, but very accurate, analytical methods have been developed to describe the helium atom in the absence of the external field [1,2]. In the presence of an intense laser field the numerical integration of Schrödinger's equation is the most effective tool to study the correlated dynamics in a two-electron system. This can be done directly [3] for the three-dimensional (3D) helium atom; however, such a calculation is feasible for only a limited range of field parameters, and anyway, it is very computationally demanding (which makes it relevant to consider a simplified 3D two-electron system [4]). Moreover, many aspects of the multielectron dynamics can be simulated via a one-dimensional (1D) helium model [5–8]. In particular, it can be used to study such dynamics in the laser field [9–19].

The existence of autoionizing states (AISs; quasistable atomic states whose excitation energies exceed the ionization threshold) is one of the striking multielectronic phenomena. The role of these states in high-order harmonic generation (HHG) is actively being studied both theoretically [20–25] and experimentally [26–30] (for a review see [31] and references therein). When the one-photon transition from an AIS to the ground state is allowed (such an AIS is called a bright one) and the transition frequency is close to the harmonic

frequency, the HHG can be strongly enhanced (by more than an order of magnitude). This can be attributed to the AIS population from the continuum in the rescattering process and XUV emission via the AIS–ground-state transition [22]. Moreover, HHG enhancement by a bright AIS *dressed* by two laser photons was observed [32].

If the transition is forbidden, the AIS is called a dark one. In particular, this is the case when the AIS has the same parity as the ground one. This AIS can be populated by an *even* number of laser photons, but the XUV at the AIS–ground-state frequency cannot be emitted. However, the dark AIS dressed by the laser photon can absorb [33,34] or emit an XUV photon. Very recently, HHG enhancement due to dressed dark AIS was observed in an indium plasma plume [35].

In this paper we study the resonant properties of HHG using the numerical integration of the time-dependent Schrödinger equation (TDSE) for 1D helium. We investigate the level structure of the 1D helium atom and ion with an emphasis on the AIS properties. Knowledge of the level structure allows attributing HHG enhancement found in numerical calculations to resonances with certain AISs. In particular, we investigate the enhancement of two neighboring odd harmonics due to a single resonance with the dark AIS. Calculating intensities and phases of these harmonics, we show that the shape of the resonant harmonic enhancement line can be linked to the attosecond properties of the resonant XUV emission.

II. LEVEL STRUCTURE OF 1D HELIUM

We integrate numerically the two-electron TDSE for 1D helium in an external field $E(t)$ (atomic units are used in all

_____
[*]strelkov.v@gmail.com

equations unless otherwise specified):

$$i\frac{\partial}{\partial t}\psi(x, y, t)$$
$$= \left[-\frac{1}{2}\frac{\partial^2}{\partial x^2} - \frac{1}{2}\frac{\partial^2}{\partial y^2} + V(x, y) + (x + y)E(t)\right]\psi(x, y, t),$$

$$(1)$$

where x and y are the electrons' coordinates and $V(x, y)$ is the atomic potential. Note that only a linearly polarized field $E(t)$ can be considered within the 1D helium model.

The atomic potential is

$$V(x, y) = \frac{-2}{\sqrt{x^2 + a^2}} + \frac{-2}{\sqrt{y^2 + a^2}} + \frac{1}{\sqrt{(x - y)^2 + b^2}}$$
$$- iV_{abs}(x) - iV_{abs}(y),$$

$$(2)$$

where a and b are constants and V_{abs} describes the wave-function absorption at the numerical box boundaries; this potential is zero everywhere except in the narrow region near the boundaries (see the Appendix). We use $a = 1/\sqrt{2} = 0.707$ and $b = 1/\sqrt{3} = 0.577$ to reproduce the first and second ionization potentials of the actual helium (see the Appendix). Note that a similar value of the latter constant was found in [17], and the former constant was found in Ref. [36]. The TDSE (1) is solved numerically with the approach described in [37]. Calculations described in this section and Sec. III use $E = 0$, while in other sections $E \neq 0$. The solution is done on a spatial grid of $N \times N$ nodes; the number N depends on the conditions: for calculations with zero field or an XUV field we use $N = 500$, and for calculations with an IR field we use $N = 1000$, so that the free wave packet oscillating in the field is described adequately. The spatial step is 0.2 a.u.; 100 nodes at the boundaries of the numerical box are occupied by the (almost nonreflecting) absorbing layers where $V_{abs} \neq 0$.

The level structures of the ion and the atom are illustrated in Fig. 1; the method for calculating the energies of the levels is described in the Appendix. We present both the binding energies of the levels (multiplied by -1) and the excitation energies with respect to the atomic ground state.

An atomic level is characterized by a pair of integer quantum numbers n_x and n_y; $n_{x,y} = 0, 1, \ldots$. The state is even if $n_x + n_y$ is even and odd if $n_x + n_y$ is odd. A quantum number can be understood as describing the state of one electron.[1] So the states $(0, n)$ are the bound atomic states. For $n \gg 1$ these are the Rydberg states. The state $(1,1)$ is the first doubly excited state. Using the modified Pöschl-Teller potential (see the Appendix), we can estimate the energy of this state in zero approximation neglecting the electron-electron interaction. Within this approximation the energy of the state is twice the energy E_1 given by Eq. (A4); this gives $2 \times -18.6\,\text{eV} = -37.2\,\text{eV}$, which is in reasonable agreement with the level energy of $-34.0\,\text{eV}$ found by numerically solving the TDSE.

_____

[1]In contrast to the 3D atom, the ground state in a one-electron 1D system is usually denoted by $n = 0$ (so that n gives the number of wave-function nodes), not $n = 1$; see, for instance, Eq. (A4). Keeping this tradition, we use $n_{x,y} = 0, 1, \ldots$ to number the states of our system.
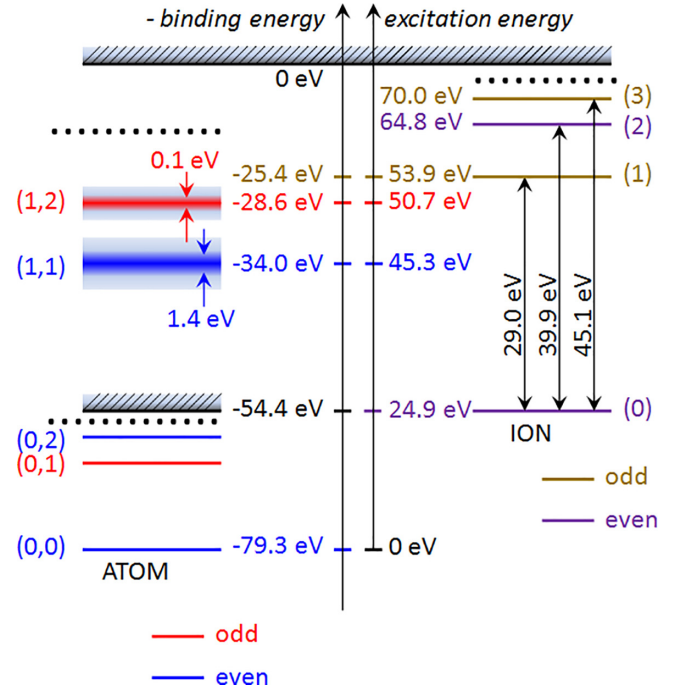

FIG. 1. The level structure of the model 1D helium atom and the 1D hydrogenlike ion. Zero of the excitation energy corresponds to the energy of the ground state of the atom; zero of the binding energy corresponds to the second ionization threshold.

III. SPATIAL DISTRIBUTION OF THE ELECTRONIC DENSITY IN THE AIS

The wave functions for several states found via the numerical TDSE solution are shown in Fig. 2, and details of the corresponding calculations are presented in Sec. A 2

Let us discuss the properties of the wave functions shown in Fig. 2. First, the potential and the wave functions are symmetric with respect to the line $y = x$. This is a result of the indistinguishability of the electrons. Note that we assume that the two electrons *can* find themselves in the same point, so we consider parahelium. Second, in Fig. 2 one can see that the ground $(0,0)$ and dark AIS $(1,1)$ states are even because the wave functions do not change sign after the inversion of the space coordinates $x \to -x$, $y \to -y$ and the first excited state $(0,1)$ is odd (see the middle and right columns in Fig. 2). Third, the AIS wave function consists of a part which is well localized near the origin and the running waves, which "leak out" from the atom along the valleys ($x = 0$ and $y = 0$) of the potential (see Fig. 10).

IV. RESONANCES WITH AUTOIONIZING STATES IN ONE- AND TWO-PHOTON IONIZATION

In this section we study the resonant features appearing in the photoelectronic spectrum due to bright and dark AISs. To calculate the photoelectronic spectrum we numerically solve the TDSE for an atom irradiated by an XUV field, thus finding the wave function as a function of space and time $\psi(x, y, t)$. Then we calculate its spectrum $\psi(x, y, \omega)$ and the energy distribution for the part of the wave function where at least
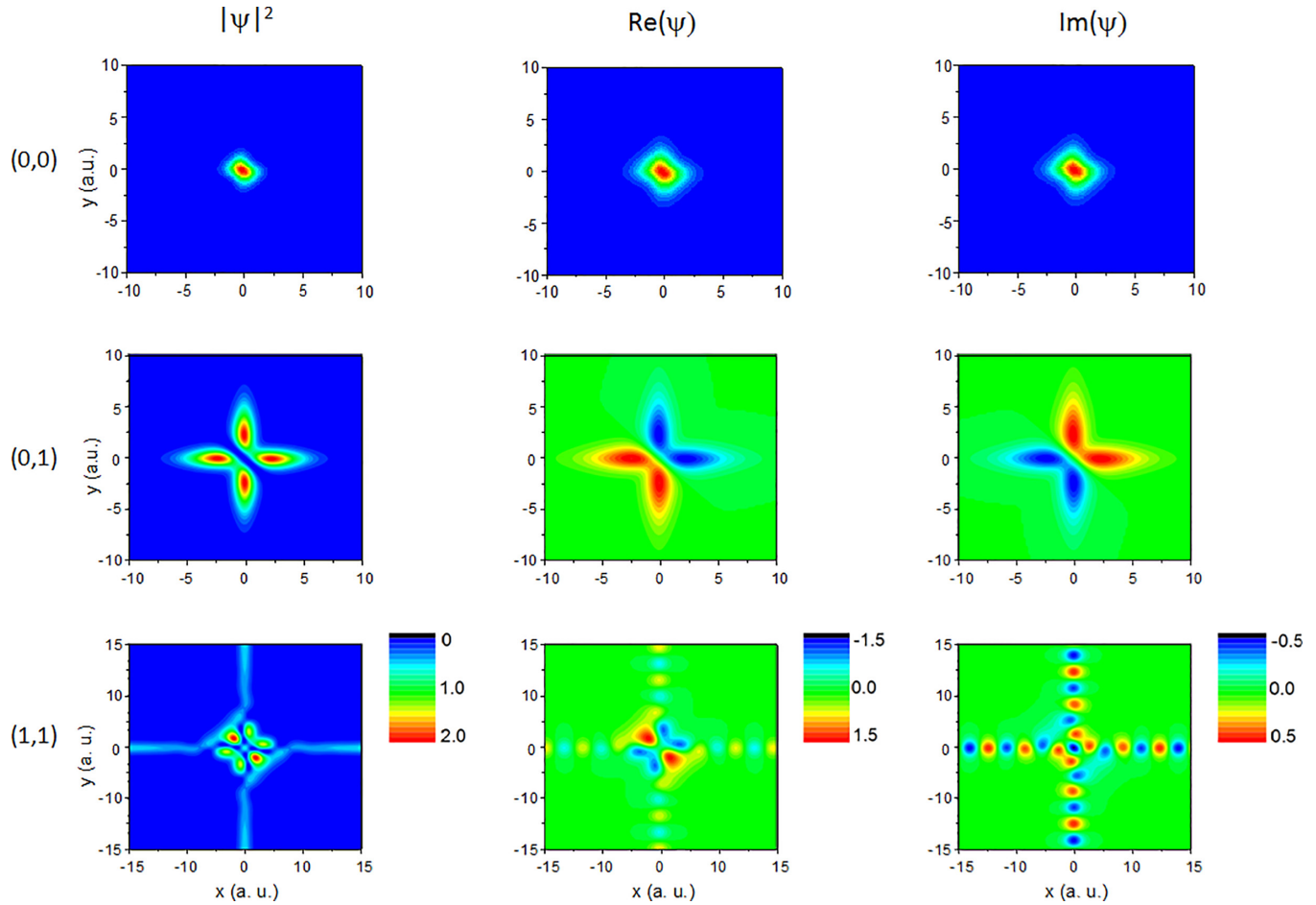
FIG. 2. Wave functions of several states in a 1D helium atom. Absolute value squared (left column) and real (middle column) and imaginary (right column) parts of the wave functions of the ground (0,0) (top row), first excited (0,1) (middle row), and lowest dark AIS (1,1) (bottom row) states. (Note the different scale in the bottom row.)

one electron is free:[2]

$$\widetilde{W}(\omega) = \int_{x^2+y^2>r^2} dxdy |\psi(x, y, \omega)|^2. \qquad (3)$$

We used $r = 30$ and checked that the results are not sensitive to this parameter provided that $r > 20$. In Eq. (3) ω is the binding energy (negative when the system is in atomic bound states or in ionic bound states plus a free electron). It is more convenient to deal with the excitation energy $\omega - E_0$, where $E_0 = -79.3$ eV is the atomic ground-state energy. In the excitation energy range between the first ionization energy (24.9 eV) and the first excited state of the ion (53.9 eV) photoionization leads to the appearance of a free electron and an ion in the ground state. So the energy

of the ion is defined; thus, the spectrum (3) directly corresponds to the photoelectron spectrum. Figure 3 presents the spectrum as a function of the excitation energy. Note that the spectra are normalized, so they are not affected by the absorption of the wave packet at the boundaries of the numerical grid.

The *bright* AISs lead to resonant features in the spectrum of the electrons detached due to *one*-photon ionization. To find this spectrum we solve the TDSE for an atom irradiated by a short XUV pulse. Its central frequency is 50.7 eV [thus close to the lowest bright AIS (1,2) excitation energy], its duration is 1.25 fs (the FWHM bandwidth is 3 eV), the peak intensity is 3.5×10^{12} W/cm^2 (the field amplitude is 0.01 a.u.), and the pulse shape is sin^2. The TDSE is solved over a time interval of 200 fs, thus over the irradiation time plus a long time after the pulse. For the short XUV pulse used here the latter time period is important for the correct photoelectron spectrum calculation because the AISs continue to decay after the pulse has already passed. Calculating the spectrum over the whole time, we find the spectrum with the Fano [38] feature appearing in the photoelectron spectrum in Fig. 3 (red line). Note that a similar feature was found in the 1D helium photoelectron spectrum in Ref. [17]. We have found the width and the Fano parameter of the line, which are shown in the graph.

---

[2]This operation requires storage of a large amount of data in computer memory; to make it less demanding, we store the wave function not at *every* step of numerical integration $dt = 0.05$, but at every eighth step. Correspondingly, we find only the lowest-energy part of the photoelectronic spectrum. This is definitely sufficient here because the inverse step of the numerical integration is much higher than reasonable electronic energies.
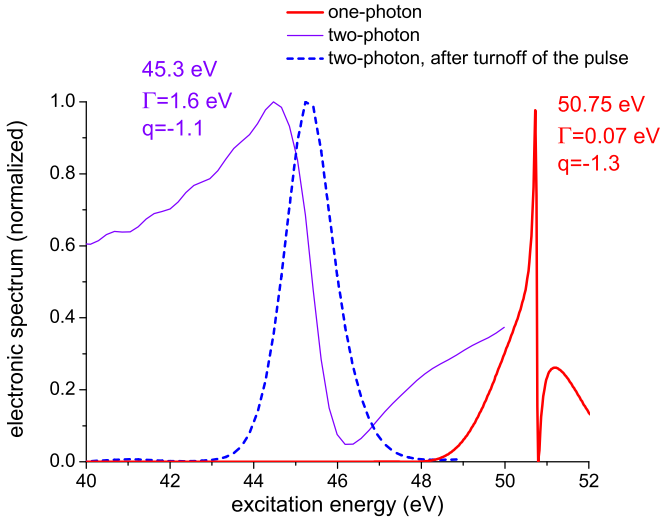
FIG. 3. Normalized photoelectron spectra calculated for the case of irradiation of the atom by one-color (thick red curve) and two-color (dashed blue and thin violet curves) XUV fields; see the text for more details. The two-photon resonance leads to a Fano feature in the total spectrum (thin violet curve) due to the interference of the resonant and nonresonant terms, whereas the resonant term can be separated by calculating the spectrum over the time interval *after* the irradiation (dashed blue curve). The central frequencies, the FWHM, and the Fano parameter of the peaks are shown in the graph.

To find the resonances with the *dark* AIS, we solve the TDSE for an atom irradiated by a *two*-color XUV pulse. The carrier frequencies are 130 and 85 eV; the pulse duration is 100 as. These frequencies of the fields are chosen to have a two-photon response in the studied spectral range (due to the Raman-type transition $130 - 85 = 45$ eV) and no one-photon response in this range. The short duration of the pulse provides the wide spectral range covered by the two-photon response (more precisely, the spectrum of the field squared has a wide peak near 45 eV, and the FWHM of this peak is 27 eV). The fields' amplitudes are 1.0 a.u. Such high amplitudes are chosen to have a pronounced yield of the two-photon process. The TDSE integration time is 50 fs. Calculating the spectrum over the whole time, we find the spectrum with the Fano feature (see the solid violet curve in Fig. 3). This feature appears due to the interference of the nonresonant and resonant contributions to the two-photon ionization; the latter contribution is due to the dark AIS. Moreover, calculating the spectrum for the time interval where the field is off, we find only the resonant contribution (see the dashed blue line).

Note that the authors of Ref. [10] studied the parameters of the Fano resonance appearing as a result of the single-photon ionization from the first atomic excited state to the dark AIS. The width of the resonance is very close to that found in our simulations (hence, the parameters of the 1D He potential in Ref. [10] are $a = b = 1$). The Fano parameter is also negative, but it is much higher; thus, the line shapes of the single-photon transition from the first excited state to the (1,1) AIS and of the two-photon transition from the ground state to the (1,1) AIS differ essentially.
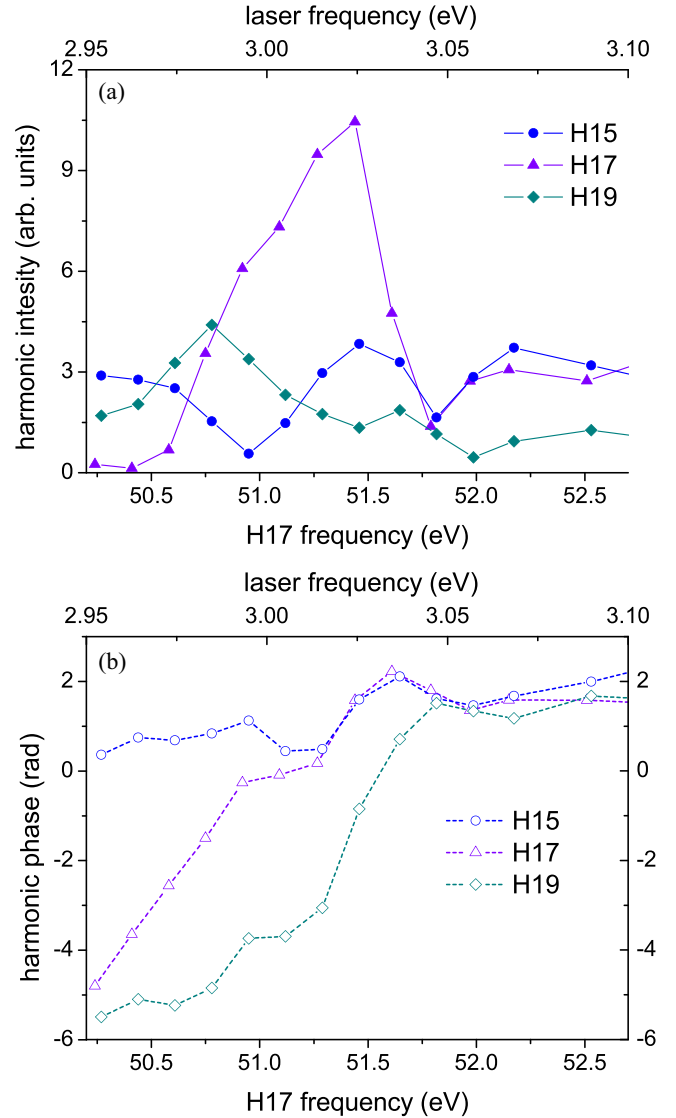

FIG. 4. (a) Intensity and (b) phase of harmonics 15 (blue circles), 17 (violet triangles), and 19 (cyan diamonds) in the vicinity of the 17-photon resonance with the bright AIS (1,2).

V. RESONANCES WITH AUTOIONIZING STATES IN HHG

In this section we study the role of resonances with the AISs in HHG simulating the XUV spectrum emitted by our model atom in an external laser field. The peak pulse intensity is 8×10^{14} W/cm^2, and the fundamental frequency ω_l is about 3 eV [the wavelength is about 400 nm, the cutoff is approximately at harmonic 19 (H19) to H21, and the Keldysh parameter is $\gamma \approx 0.95$]; it is tuned near the 14th-order resonance with the transition from the ground state to the dark (1,1) AIS and near the 17th-order resonance with the bright (1,2) AIS. The laser pulse intensity increases for four cycles, and then it is constant for eight cycles and then decreases down to zero for four cycles; the slopes of the pulse have sin^2 shape.

In Fig. 4 we show the intensities and phases of H15, H17, and H19 as a function of laser frequency (the horizontal axis above the graph) in the vicinity of the resonance with the
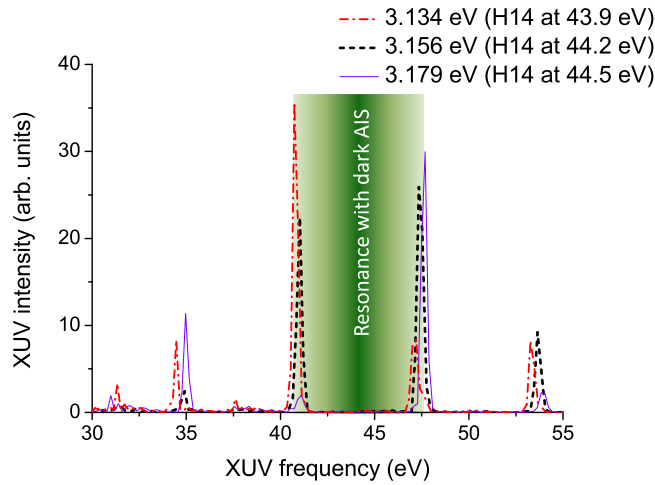
FIG. 5. HHG spectra in the vicinity of the 14-photon resonance with the dark AIS (1,1). The fundamental frequency and the frequency of harmonic 14 is shown in the graph.

bright AIS. The H17 frequency is shown for reference in the axis below the graph. We can see a pronounced enhancement of the resonant harmonic intensity. The "enhancement line" (enhancement as a function of the laser frequency) is shifted and broadened with respect to the resonant line in the one-photon photoelectron spectrum shown in Fig. 3. This can be attributed to the line modification by the laser field (to the Stark shift of the levels and photoionization of the AIS).[3] Moreover, there is even a qualitative difference between the shapes of the lines in the photoelectronic spectrum and harmonic enhancement: in the spectrum the dip is on the high-energy side of the maximum; in the enhancement line it is on the low-energy side. This agrees with experimental studies on HHG in helium: in the photoabsorption spectrum [41] the dip is on the high-energy side, and in the XUV spectrum [27] it is on the low-energy one. A similar difference was discussed in [24].

One can also see a pronounced modification of the harmonic phase by the resonance; such distortion was measured in [42]. Also there is some enhancement of the harmonic above the resonance (H19) and almost no enhancement of the harmonic below it (H15). However, the phases of all three harmonics are affected by the resonance. The total variation of the laser frequency in Fig. 4 is small (approximately 5%), so the nonresonant contribution to the generation of a harmonic should not vary much; the resonant one vanishes at the edges of the considered frequency range. Thus, the total phase variation over this range for a harmonic is approximately either zero or 2π.

---

[3]Note that the Stark shift of the ground-state energy can be estimated [39] as $-\alpha E^2/2$, where α is the polarizability of the atom. Using the experimental polarizability from [40], we find that the shift in the used field is about 0.5 eV. This value can be used as an order-of-magnitude estimation of the Stark shifts of the transition frequencies. The value of the resonant frequency shift in Fig. 4 agrees with this estimation.
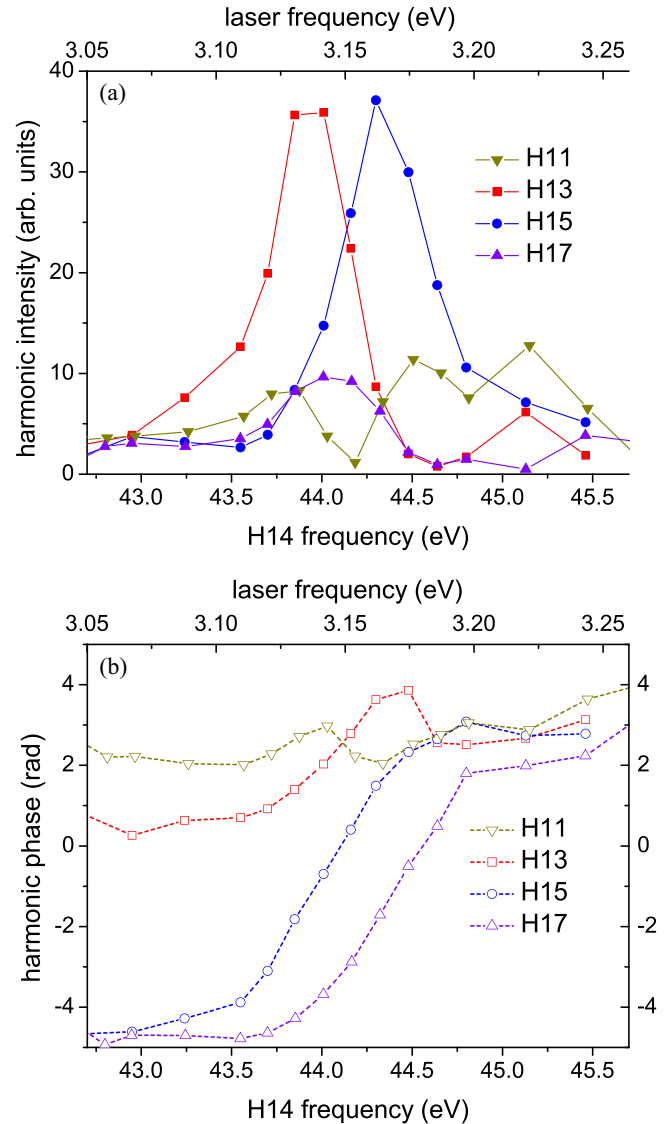

FIG. 6. (a) Intensity and (b) phase of harmonics 11 (yellow triangles), 13 (red squares), 15 (blue circles), and 17 (violet triangles) in the vicinity of the 14-photon resonance with the dark AIS (1,1).

The HHG modification by the dark AIS has been studied much less than that for the bright AIS. Very recently, the resonance of an even number of laser photons with the dark AIS was considered [35], and an enhancement of the harmonic with an order differing by unity from this number was observed. This phenomenon can be understood as a resonance between the harmonic and the dark AIS, dressed by a laser photon.

Our simulations presented in Fig. 5 show that in the case of the 14th-order resonance with the dark AIS the two neighboring harmonics (i.e., H13 and H15) are enhanced by the resonance. Note that there are no one-photon resonances that can cause the HHG enhancement in the considered spectral range (see Fig. 3).

To study this enhancement in more detail we present in Fig. 6 the intensity of H13 and H15 as a function of the fundamental frequency in the vicinity of the 14-photon resonance with the dark AIS. Comparing Fig. 6 with Fig. 4, we can see

that the enhancements caused by the resonances with dark and bright AISs are comparable in the considered conditions. The width of the enhancement lines for H13 and H15 are close to the one in the two-photon photoelectron spectrum in Fig. 3; the center of the HHG enhancement line is slightly shifted due to the Stark shift of the levels in the laser field. Counterintuitively, the enhancement lines for H13 (red) and H15 (blue) are different: the peak enhancement is achieved for different laser frequencies; moreover, zero enhancement for H13 near 44.6 eV does not correspond to any specific feature of H15 at this frequency.

The difference in the enhancement lines for H13 and H15 can be understood by taking into account that XUV emission time is different under resonant and nonresonant conditions: one can assume that, similar to the HHG enhancement with the bright AIS, the resonant XUV emission is delayed (with respect to the nonresonant one) by the AIS lifetime [43,44]. In more detail, the difference in the harmonic enhancement lines can be explained as follows.

Similar to the Fano line in the photoionization cross section, the harmonic enhancement line originates from the interference of the resonant and nonresonant terms [24] in the harmonic amplitude. The phase of the resonant term varies strongly near the resonance as a function of the detuning, whereas the phase of the nonresonant term does not. Let us denote the phase difference of these terms for the qth harmonic as

$$\delta\varphi_q = \varphi_q^r - \varphi_q^{nr}. \tag{4}$$

The difference in the H15 and H13 phases $\Delta\varphi = \varphi_{15} - \varphi_{13}$ defines the emission time [45] of the attosecond pulse consisting of H15 and H13: $t_e = \Delta\varphi/(2\omega_l)$. (Note that $\Delta\varphi$ should not be confused with $\delta\varphi_q$: the former gives the phase difference between the neighboring harmonics, whereas $\delta\varphi_q$ describes the interference of the resonant and nonresonant terms of the same harmonic.)

Far from the resonance the nonresonant term dominates: $\varphi_q \approx \varphi_q^{nr}$, so the emission time is defined by this term:

$$\Delta\varphi^{nr} = \varphi_{15}^{nr} - \varphi_{13}^{nr} = 2t_e^{nr}\omega_l. \tag{5}$$

Note that the phases of the nonresonant terms do not vary much within the considered small detuning interval of the fundamental; in particular, this equation is valid near the resonance as well.

Near the resonance the resonant term dominates: $\varphi_q \approx \varphi_q^r$, so the emission time is defined by this term. This emission time, as we mentioned above, is $t_e^r = t_e^{nr} + \tau$, where τ is the AIS lifetime. So near the resonance

$$\Delta\varphi^r = \varphi_{15}^r - \varphi_{13}^r = 2(t_e^{nr} + \tau)\omega_l. \tag{6}$$

From Eqs. (4), (5), and (6) we conclude that near the resonance $\delta\varphi_{15} - \delta\varphi_{13} = 2\tau\omega_l$. So the enhancement line shapes defined by the interference of resonant and nonresonant contributions to the harmonic emission are different for H13 and H15.

From the harmonic phases shown in Fig. 6 we find that $\Delta\varphi^{nr} \approx 0$ and $\Delta\varphi^r \approx 2.8$ rad. From Eqs. (5) and (6) we find $\tau = 300$ as. This agrees with the fact that this delay is comparable to but less than the inverse FWHM of the resonant term
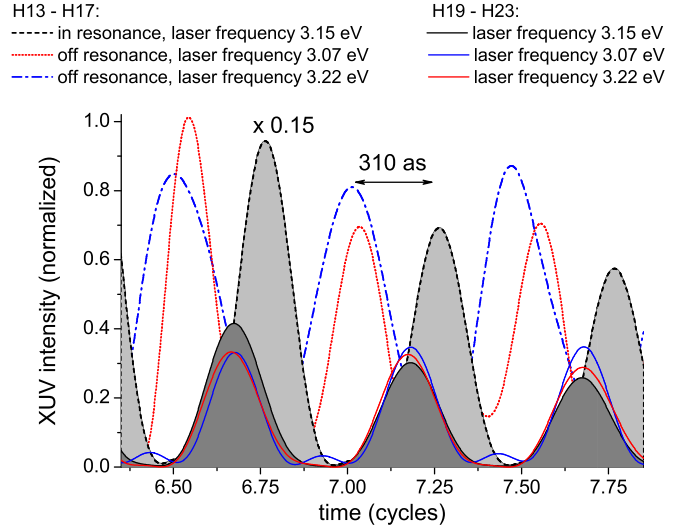

FIG. 7. Attosecond pulses produced by the harmonics near the resonance with the dark AIS (dashed, dotted, and dash-dotted lines) and by the cutoff harmonics (solid lines) for the three fundamental frequencies shown in the graph.

in the two-photon ionization cross section (blue line in Fig. 3), namely, $1/\Gamma = 470$ as.

Note that in Ref. [42] the resonant phase was measured under some detuning from the resonance because closer to the resonance the intensity difference between the resonant and nonresonant harmonics makes RABBIT (reconstruction of attosecond beating by interference of two-photon transitions) measurements problematic. For HHG enhanced by the dark AIS such measurements can be done near the center of the resonance because the *two* harmonics are enhanced in a similar way.

Figure 7 shows the attosecond pulses obtained from the cutoff harmonics (H19–H23) and harmonics near the 14-photon resonance with dark AIS (H13–H17). Naturally, the emission time of the cutoff attosecond pulse does not depend on the detuning from the resonance. So this emission time gives a straightforward reference for the emission times of the attosecond pulses obtained from H13 to H17. The latter pulses in the off-resonance conditions are emitted before the cutoff attosecond pulse. (This shows that the short quantum path dominates in HHG response; see [45].) The H13–H17 pulses are emitted approximately at the same time for the above-resonance conditions (laser frequency of 3.22 eV) and the below-resonance ones (laser frequency of 3.07 eV), so the resonance does not affect the attosecond pulses emission. In the resonant case the attosecond pulse is much more intense and emitted later than in the off-resonant cases, in agreement with the considerations presented above. The delay of 310 as is close to the one found above from the harmonic phases.

VI. CONCLUSIONS

In this paper we studied the role of dark and bright AISs in resonant HHG using the 1D helium model allowing *ab initio* numerical TDSE simulations beyond the single-electron approximation.

The analytical model using a modified Pöschl-Teller potential allowed us to obtain a reasonable estimate of the lowest doubly excited state energy. We presented the structure of the (lowest) levels of the studied system. The simplicity of the system allows straightforward graphical presentation of the wave functions of different states, including the AI ones.

We made detailed simulations of the interaction of the atom with electromagnetic field. The photoelectronic spectra demonstrated pronounced features due to resonances with AISs. In particular, the resonances lead to asymmetric Fano peaks in the spectrum of the photoelectrons appearing due to one- and two-photon ionization.

We simulated the HHG enhancement via the resonance with the bright AIS and found a pronounced difference between the shapes of the above-mentioned Fano maximum in the photoelectronic spectrum and the harmonic enhancement line. We found an essential enhancement of the resonant harmonic, some enhancement of the harmonic above it, and no enhancement of the harmonic below it.

Moreover, we simulated HHG under the conditions in which the fundamental frequency is close to a multiphoton resonance of an even order with the dark AIS. We found enhanced generation of the neighboring harmonics. The shapes of the enhancement lines for the harmonics are different. The difference can be understood by taking into account the harmonic phase properties defined by a delay between the nonresonant and resonant XUV emissions; this delay is close to the AIS lifetime. Simultaneous enhancement of the two harmonics by the resonance with the dark AIS makes the experimental measurement of resonance-induced dephasing between them feasible. Finally, our simulations showed that the HHG enhancement rates due to resonances with the dark and bright AISs are comparable in the studied system.

ACKNOWLEDGMENTS

APPENDIX

1. One-dimensional hydrogenlike ion

A 1D hydrogen atom or hydrogenlike ion with a Coulomb potential or a soft-Coulomb potential was studied in a number of papers [46–51]. In contrast to the 3D system, the bound state of the 1D hydrogen cannot be found analytically for either the Coulomb or soft-Coulomb potential. Here we describe our numerical method and approximate an analytical approach to find the eigenstates' energies and wave functions.

To study a He^+ ion we remove the electron-electron repulsion term in Eq. (2). Then the TDSE describes two non-
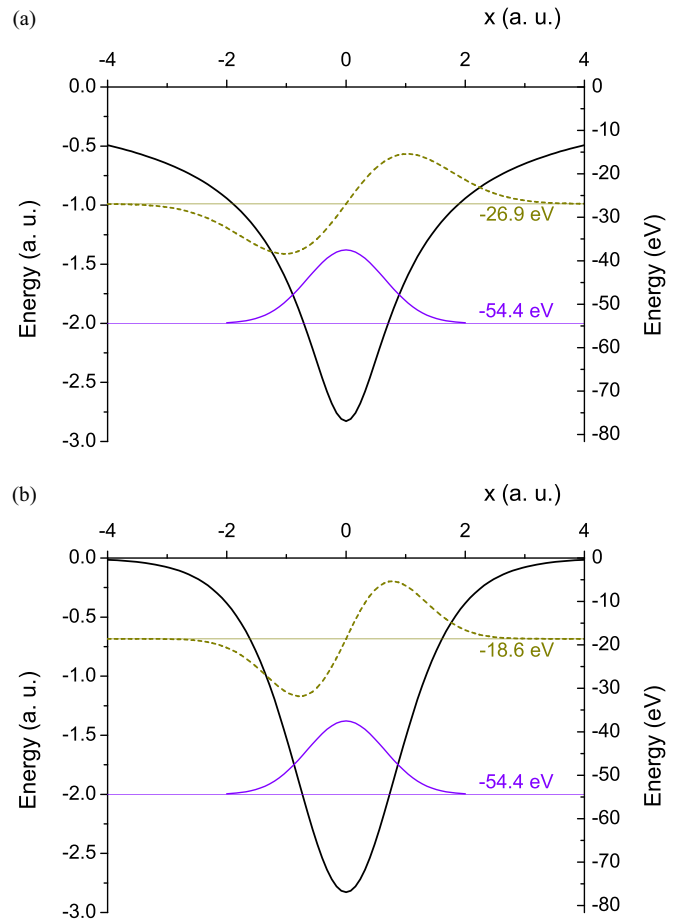

FIG. 8. (a) Soft-Coulomb and (b) modified Pöschl-Teller potentials. Thin solid and dashed lines show the ground- and first-excited-state wave -functions, respectively.

interacting ions, and the interpretation of the TDSE solution results in terms of a single ion is straightforward. The ion's potential is

$$V_{\text{ion}}(x) = \frac{-2}{\sqrt{x^2 + a^2}} - iV_{\text{abs}}(x). \tag{A1}$$

Under $a = 1/\sqrt{2}$ the ground-state energy of the model ion is equal to the actual ionization energy of He^+ [36]. The soft-Coulomb potential [the first term in Eq. (A1)] is shown in Fig. 8(a), and the absorbing potential (the second term) is shown in Fig. 9. The absorption is zero in the central part of the numerical box and turns on softly for $|x| > x_{\text{abs}}$. We choose $x_{\text{abs}} = x_0 - 100dx$ (x_0 is the boundary position and $dx = 0.2$ is the spatial step of the TDSE integration) and $V_{\text{abs}}^{\max} = 0.1/dt$ ($dt = 0.05$ is the temporal step). A soft increase of the absorption for $|x| > x_{\text{abs}}$ in conjunction with the proper choice of x_{abs} and $V_{\text{abs}}^{\max}$ provides vanishing reflection for different wavelengths.

Solving the TDSE, we find the energies of the ground state and several first excited ones. The energy and wave functions of the states are found as follows. The initial wave function of the nth state ($n = 0, 1, \dots$) is set as the corresponding wave function of a harmonic oscillator; then the wave-function evolution is simulated with a numerical TDSE solution.
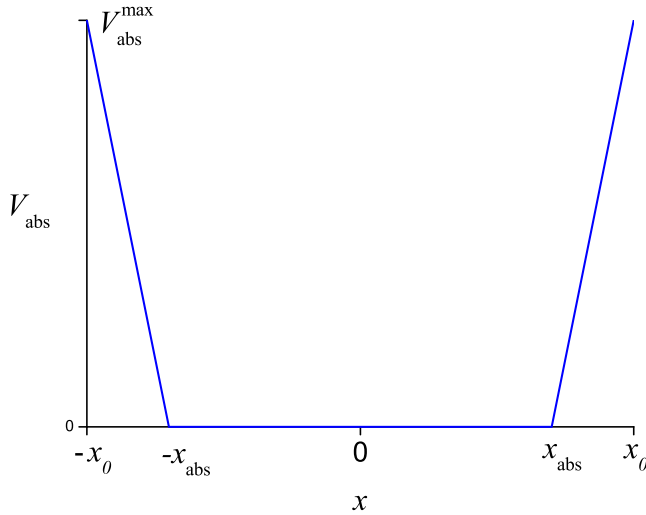
FIG. 9. The absorbing potential used in the numerical TDSE solution. See the text for more details.

FIG. 10. Potential given by Eq. (2) describing the model 1D helium atom.

The part of the initial wave function that is orthogonal to the bound eigenstates of the ion spreads in space and finally is absorbed by the absorbing boundary of the numerical box. So the part of the wave function bound near the origin corresponds to the eigenstate of the potential (A1) (more precisely, it corresponds to a superposition of the eigenstates; however, choosing the initial wave function with a proper number of zeros guarantees that the weight of all eigenstates except one is very small). The numerical TDSE solution gives us the wave function as a function of space and time $\psi(x, y, t)$. We calculate its spectrum $\psi(x, y, \omega)$ and the following energy distribution:

$$W(\omega) = \int dx dy |\psi(x, y, \omega)|^2. \quad (A2)$$

(In contrast to Eq. (3), here the integration is done over the whole numerical box.) The energy of the maximum in this distribution gives the energy of the found state; this negative energy is the state's binding energy, multiplied by -1. Other peaks in the energy distribution, if any, are much weaker; the ratio of the peaks to the main one gives the weights of the other eigenstates in the found state. (In our calculations the difference was six orders of magnitude when finding the wave function of the ground state and more than four orders of magnitude when finding wave functions of the first and second excited states.)

In [46] the approximate equation for the ground states' energies of the truncated Coulomb potential was found. The accuracy of the approximation becomes better as the truncation parameter (roughly analogous to the parameter a) tends to zero. However, under $a = 1/\sqrt{2}$ the accuracy for the ground and first excited states is insufficient. A much better analytical approach can be developed by approximating the soft-Coulomb potential (A1) with the modified Pöschl-Teller potential:

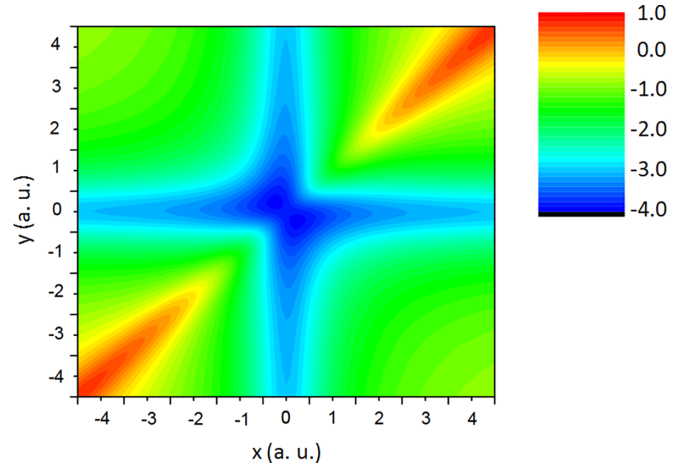$$V_{PT}(x) = -\frac{\alpha^2}{2} \frac{\lambda(\lambda - 1)}{\cosh^2(\alpha x)}, \quad (A3)$$

where α and λ are parameters. The bound states' energies for this potential are [52]

$$E_n = -\frac{\alpha^2}{2}(\lambda - 1 - n)^2,$$
$$n = 0, 1, \ldots,$$
$$n \leqslant \lambda - 1, \quad (A4)$$

and an even n gives the energy of an even state, and an odd n gives the energy of an odd one.

The parameters α and λ are chosen so that (i) the minimum of the potential (A3) is equal to the minimum of the potential (A1) and (ii) the energy of the ground state E_0 is equal in both potentials. The obtained approximated potential is shown in Fig. 8(b). Using Eq. (A4), we find the energy of the first excited state $E_1 = -18.6$ eV.

2. One-dimensional helium: Calculation of the electronic density spatial distribution in the AIS

Setting $b \approx a$ in potential (2), we consider a two-electron atom. The parameter b is chosen so that the atom ionization energy is close to that of real helium. The found value is $b = 1/\sqrt{3} = 0.577$. The energy of the atomic ground state is the energy of the ionic ground state (-54.4 eV) minus the ionization energy 24.9 eV (24.6 eV in actual helium); the found energy of the ground state is -79.3 eV. The potential given by Eq. (2) under $a = 1/\sqrt{2}$ and $b = 1/\sqrt{3}$ is shown in Fig. 10.

To find analytically the energy of the (1,1) state in the zero approximation one can neglect the electronic interaction. Within this approximation the energy of the state is double the energy E_1 given by Eq. (A4); this gives 2×-18.6 eV $= -37.2$ eV. This is pretty close to the level energy of -34.0 eV found by numerically solving TDSE. This similarity can be explained as follows: for $n \geqslant 1$ the 1D soft-Coulomb potential's levels are lower than those of the modified Pöschl-Teller potential. However, the electronic repulsion in the atom moves them up. So, finally, these two "shifts" partly compensate each other for $n = 1$. The wave functions for several

states found via the numerical TDSE solution are shown in Fig. 2.

The wave functions and the energies of the bound states (the top and middle rows in Fig. 2) are found similarly to those in the case of the hydrogenlike ion: the initial wave function for a state (n_x, n_y) is set as a symmetrized product of the one-electron wave functions (n_x) and (n_x) in the modified Pöschl-Teller potential; TDSE is solved for a long enough time that the eigenstate survives and the remaining part of the initial wave function is absorbed after spreading. The maximum in the energy distribution (A2) gives the eigenstate energy.

However, this procedure cannot be applied directly for an AIS: this state decays, so after some time we find zero population in all states. So the procedure is slightly modified. First, we set the initial wave function (1,1) as described above and propagate the TDSE for a long enough time so that the wave-function norm vanishes. Then using the wave function found during the TDSE integration $\psi(x, y, t)$, we calculate the spectrum $\psi(x, y, \omega)$. The energy of its maximum is the AIS energy E_{AIS}. Finally, we find the spatial distribution of the spectral component with this energy: $\Psi(x, y) \equiv \psi(x, y, \omega = E_{AIS})$. This function is shown in Fig. 2 (bottom row).

[1] H. Bethe and E. Salpeter, *Quantum Mechanics of One- and Two-Electron Atoms* (Springer, New York, 1957).

[2] G. Tanner, K. Richter, and J.-M. Rost, The theory of two-electron atoms: Between ground state and complete fragmentation, Rev. Mod. Phys. **72**, 497 (2000).

[3] E. S. Smyth, J. S. Parker, and K. Taylor, Numerical integration of the time-dependent Schrödinger equation for laser-driven helium, Comput. Phys. Commun. **114**, 1 (1998).

[4] C. Ruiz, L. Plaja, L. Roso, and A. Becker, *Ab Initio* Calculation of the Double Ionization of Helium in a Few-Cycle Laser Pulse Beyond the One-Dimensional Approximation, Phys. Rev. Lett. **96**, 053001 (2006).

[5] Y. Nogami, M. Vallières, and W. van Dijk, Hartree–Fock approximation for the one-dimensional "helium atom," Am. J. Phys. **44**, 886 (1976).

[6] D. K. Harriss and F. Rioux, A simple Hartree SCF calculation on a one-dimensional model of the He atom, J. Chem. Educ. **57**, 491 (1980).

[7] A. López-Castillo, M. A. M. de Aguiar, and A. M. O. de Almeida, On the one-dimensional helium atom, J. Phys. B **29**, 197 (1996).

[8] V. Skobelev, Ground state energy of a one-dimensional helium atom, Russ. Phys. J. **61**, 887 (2018).

[9] R. Grobe and J. H. Eberly, Photoelectron Spectra for a Two-Electron System in a Strong Laser Field, Phys. Rev. Lett. **68**, 2905 (1992).

[10] S. L. Haan, R. Grobe, and J. H. Eberly, Numerical study of autoionizing states in completely correlated two-electron systems, Phys. Rev. A **50**, 378 (1994).

[11] D. Bauer, Two-dimensional, two-electron model atom in a laser pulse: Exact treatment, single-active-electron analysis, time-dependent density-functional theory, classical calculations, and nonsequential ionization, Phys. Rev. A **56**, 3028 (1997).

[12] D. G. Lappas and R. van Leeuwen, Electron correlation effects in the double ionization of He, J. Phys. B **31**, L249 (1998).

[13] M. Lein, E. K. U. Gross, and V. Engel, Intense-Field Double Ionization of Helium: Identifying the Mechanism, Phys. Rev. Lett. **85**, 4707 (2000).

[14] G. D. Borisova, V. Stooß, A. Dingeldey, A. Kaldun, T. Ding, P. Birk, M. Hartmann, T. Heldt, C. Ott, and T. Pfeifer, Strong-field-induced single and double ionization dynamics from single and double excitations in a two-electron atom, J. Phys. Commun. **4**, 055012 (2020).

[15] E. A. Volkova, V. V. Gridchin, A. M. Popov, and O. V. Tikhonova, Ionization and stabilization of a two-electron atom

in a strong electromagnetic field, J. Exp. Theor. Phys. **99**, 320 (2004).

[16] L. Roso, L. Plaja, P. Moreno, E. Jarque, J. Vazquez de Aldana, J. San Román, and C. Ruiz, Multielectron atomic models using the rochester one-dimensional potential, Laser Phys. **15**, 1393 (2005).

[17] J. Zhao and M. Lein, Probing Fano resonances with ultrashort pulses, New J. Phys. **14**, 065003 (2012).

[18] P. Koval, F. Wilken, D. Bauer, and C. H. Keitel, Nonsequential Double Recombination in Intense Laser Fields, Phys. Rev. Lett. **98**, 043904 (2007).

[19] D. K. Efimov, A. Maksymov, J. S. Prauzner-Bechcicki, J. H. Thiede, B. Eckhardt, A. Chacón, M. Lewenstein, and J. Zakrzewski, Restricted-space *ab initio* models for double ionization by strong laser pulses, Phys. Rev. A **98**, 013405 (2018).

[20] D. B. Milošević, High-energy stimulated emission from plasma ablation pumped by resonant high-order harmonic generation, J. Phys. B **40**, 3367 (2007).

[21] I. A. Ivanov and A. S. Kheifets, Resonant enhancement of generation of harmonics, Phys. Rev. A **78**, 053406 (2008).

[22] V. Strelkov, Role of Autoionizing State in Resonant High-Order Harmonic Generation and Attosecond Pulse Production, Phys. Rev. Lett. **104**, 123901 (2010).

[23] M. V. Frolov, N. L. Manakov, and A. F. Starace, Potential barrier effects in high-order harmonic generation by transition-metal ions, Phys. Rev. A **82**, 023424 (2010).

[24] V. V. Strelkov, M. A. Khokhlova, and N. Y. Shubin, High-order harmonic generation and Fano resonances, Phys. Rev. A **89**, 053833 (2014).

[25] I. S. Wahyutama, T. Sato, and K. L. Ishikawa, Time-dependent multiconfiguration self-consistent-field study on resonantly enhanced high-order harmonic generation from transition-metal elements, Phys. Rev. A **99**, 063420 (2019).

[26] R. A. Ganeev, M. Suzuki, M. Baba, H. Kuroda, and T. Ozaki, Strong resonance enhancement of a single harmonic generated in the extreme ultraviolet range, Opt. Lett. **31**, 1699 (2006).

[27] S. Gilbertson, H. Mashiko, C. Li, E. Moon, and Z. Chang, Effects of laser pulse duration on extreme ultraviolet spectra from double optical gating, Appl. Phys. Lett. **93**, 111105 (2008).

[28] M. Singh, M. A. Fareed, V. Strelkov, A. N. Grum-Grzhimailo, A. Magunov, A. Laramée, F. Légaré, and T. Ozaki, Intense quasi-monochromatic resonant harmonic generation in the multiphoton ionization regime, Optica **8**, 1122 (2021).

[29] A. D. Shiner, B. E. Schmidt, C. Trallero-Herrero, H. J. Wörner, S. Patchkovskii, P. B. Corkum, J.-C. Kieffer, F. Légaré, and

D. M. Villeneuve, Probing collective multi-electron dynamics in xenon with high-harmonic spectroscopy, Nat. Phys. **7**, 464 (2011).

[30] M. A. Fareed, V. V. Strelkov, M. Singh, N. Thiré, S. Mondal, B. E. Schmidt, F. Légaré, and T. Ozaki, Harmonic Generation from Neutral Manganese Atoms in the Vicinity of the Giant Autoionization Resonance, Phys. Rev. Lett. **121**, 023201 (2018).

[31] R. Ganeev, Harmonic generation in laser-produced plasmas containing atoms, ions and clusters: A review, J. Mod. Opt. **59**, 409 (2012).

[32] M. A. Fareed, V. V. Strelkov, N. Thiré, S. Mondal, B. E. Schmidt, F. Légaré, and T. Ozaki, High-order harmonic generation from the dressed autoionizing states, Nat. Commun. **8**, 16061 (2017).

[33] A. I. Magunov, I. Rotter, and S. I. Strakhova, Laser-induced continuum structures and double poles of the s-matrix, J. Phys. B **34**, 29 (2001).

[34] L. Argenti, A. Jiménez-Galán, C. Marante, C. Ott, T. Pfeifer, and F. Martín, Dressing effects in the attosecond transient absorption spectra of doubly excited states in helium, Phys. Rev. A **91**, 061403(R) (2015).

[35] M. Singh, M. A. Fareed, V. Birulia, A. Magunov, A. N. Grum-Grzhimailo, P. Lassonde, A. Laramée, R. Marcelino, R. G. Shirinabadi, F. Légaré, T. Ozaki, and V. Strelkov, Ultrafast Resonant State Formation by the Coupling of Rydberg and Dark Autoionizing States, Phys. Rev. Lett. **130**, 073201 (2023).

[36] J. Javanainen, J. H. Eberly, and Q. Su, Numerical simulations of multiphoton ionization and above-threshold electron spectra, Phys. Rev. A **38**, 3430 (1988).

[37] V. V. Strelkov, A. F. Sterjantov, N. Y. Shubin, and V. T. Platonenko, XUV generation with several-cycle laser pulse in barrier-suppression regime, J. Phys. B **39**, 577 (2006).

[38] U. Fano, Effects of configuration interaction on intensities and phase shifts, Phys. Rev. **124**, 1866 (1961).

[39] L. D. Landau and E. M. Lifshitz, *Quantum Mechanics*, 3rd ed., Course of Theoretical Physics Vol. 3 (Pergamon, England, 1973), Sec. 76.

[40] K. T. Chung, Dynamic polarizability of helium, Phys. Rev. **166**, 1 (1968).

[41] W. F. Chan, G. Cooper, and C. E. Brion, Absolute optical oscillator strengths for the electronic excitation of atoms at high resolution: Experimental methods and measurements for helium, Phys. Rev. A **44**, 186 (1991).

[42] S. Haessler, V. Strelkov, L. B. E. Bom, M. Khokhlova, O. Gobert, J.-F. Hergott, F. Lepetit, M. Perdrix, T. Ozaki, and P. Salières, Phase distortions of attosecond pulses produced by resonance-enhanced high harmonic generation, New J. Phys. **15**, 013051 (2013).

[43] M. Tudorovskaya and M. Lein, High-order harmonic generation in the presence of a resonance, Phys. Rev. A **84**, 013430 (2011).

[44] V. V. Strelkov, Attosecond-pulse production using resonantly enhanced high-order harmonics, Phys. Rev. A **94**, 063420 (2016).

[45] Y. Mairesse, A. de Bohan, L. J. Frasinski, H. Merdji, L. C. Dinu, P. Monchicourt, P. Breger, M. Kovačev, R. Taïeb, B. Carré, H. G. Muller, P. Agostini, and P. Salières, Attosecond synchronization of high-harmonic soft x-rays, Science **302**, 1540 (2003).

[46] R. Loudon, One-dimensional hydrogen atom, Am. J. Phys. **27**, 649 (1959).

[47] G. Palma and U. Raff, The one-dimensional hydrogen atom revisited, Can. J. Phys. **84**, 787 (2006).

[48] R. L. Hall, N. Saad, K. D. Sen, and H. Ciftci, Energies and wave functions for a soft-core coulomb potential, Phys. Rev. A **80**, 032507 (2009).

[49] R. Loudon, Proc. R. Soc. A **472**, 20150534 (2016).

[50] S. Majorosi, M. G. Benedict, and A. Czirják, Improved one-dimensional model potentials for strong-field simulations, Phys. Rev. A **98**, 023401 (2018).

[51] C. Li, Exact analytical solution of the ground-state hydrogenic problem with soft Coulomb potential, J. Phys. Chem. A **125**, 5146 (2021).

[52] S. Flügge, *Practical Quantum Mechanics II* (Springer, Berlin, 1971).